



# Component controlled synthesis of bimetallic PdCu nanoparticles supported on reduced graphene oxide for dehydrogenation of dodecahydro-*N*-ethylcarbazole

Bin Wang<sup>a</sup>, Tie-yan Chang<sup>b</sup>, Zhao Jiang<sup>a,\*</sup>, Jin-jia Wei<sup>a</sup>, Tao Fang<sup>a,\*\*</sup>

<sup>a</sup> Shaanxi Key Laboratory of Energy Chemical Process Intensification, School of Chemical Engineering and Technology, Xi'an Jiaotong University, Xi'an, 710049, China

<sup>b</sup> MOE Key Laboratory for Nonequilibrium Synthesis and Modulation of Condensed Matter, School of Science, Xi'an Jiaotong University, Xi'an, 710049, China

## ARTICLE INFO

### Keywords:

Liquid organic hydrogen carrier  
Dodecahydro-*N*-ethylcarbazole  
Dehydrogenation catalysis  
Dehydrogenation kinetics

## ABSTRACT

The unsatisfactory performance with high precious metal dosage of dehydrogenation catalysts has been the bottleneck for the development of liquid organic hydrogen carrier (LOHC). The most representative dodecahydro-*N*-ethylcarbazole in LOHC also faces the same problem. Here, we report a series of bimetallic PdCu catalysts with different ratios supported on reduced graphene oxide prepared by a facile one-pot synthesis method. The most cost-effective Pd<sub>1.2</sub>Cu/rGO catalyst with the lowest amount of precious metals in the catalysts reported for dehydrogenation of dodecahydro-*N*-ethylcarbazole was selected from a series of samples, while maintaining the catalytic activity and selectivity to the final product of *N*-ethylcarbazole as the Pd/rGO catalyst with the highest activity in recently reported studies. At the same time, the change of Pd and Cu content and the effect of preparation temperature on dehydrogenation performance were also studied, and the corresponding reaction kinetics were revealed. In combination with various characterization methods of catalyst, the relationship between structure and properties of PdCu NPs was explored in depth. The average particle size and electron transfer between Pd and Cu were identified as the key factors affecting the catalytic activity.

## 1. Introduction

The irreversible momentum of clean energy has emerged in the last decade [1]. In the past few decades of research, significant progress have been made in finding alternative energy sources with low pollutant emissions and affordable costs [2]. As a highly attractive form of energy, hydrogen stands out in alternative energy strategies that enable safe and clean energy applications [3,4]. The source of hydrogen is very extensive, and large-scale industrial hydrogen production has been going on for decades [5]. Fuel cell is a new application scenario for hydrogen that is currently under development and promoted by various countries. Due to the low density of hydrogen, its storage needs to be greatly compressed; and due to the presence of hydrogen embrittlement, the current gas pipeline delivery system cannot be used for the delivery of pure hydrogen [6]. These make hydrogen's storage and transportation the bottleneck which restrict the breakthrough development of the commercialization of hydrogen fuel cells. At present, high-pressure gaseous storage and low-temperature liquefaction storage are two mature technologies which can meet the energy density

requirements for hydrogen storage systems of US Department of Energy (gravimetric capacity of 5.5 wt% and volumetric capacity of 40 g/L) [7]. However, high cost of the equipment and excessive self-weight are the main disadvantages as on-board hydrogen source systems. In this respect, chemical hydrogen storage is an attractive alternative for on-board energy storage [8,9], especially the liquid organic hydrogen carrier (LOHC) for hydrogenation / dehydrogenation cycle storage system [4,10]. It was first proposed and initiated extensive research in the 1990s and has now evolved into a very promising technology for storing and transporting hydrogen energy, especially the *N*-ethylcarbazole (NEC) and dodecahydro-*N*-ethylcarbazole (12H-NEC) cycle systems proposed by Pez et al. in 2006, which was the earliest proposed LOHC system that can undergo hydrogen storage cycle below 473 K [11–13]. Its hydrogen storage capacity can reach 5.79 wt% in the hydrogen-rich type of 12H-NEC (Reaction pathways, see Supporting Information Fig. S1). The purity of released hydrogen can reach 99.99% [14].

Hydrogenation of NEC is a simple reaction that can be easily converted to 12H-NEC at 433–463 K and 6–9 MPa within a short time using

\* Corresponding author.

\*\* Corresponding author.

E-mail addresses: [jiangzhao@mail.xjtu.edu.cn](mailto:jiangzhao@mail.xjtu.edu.cn) (Z. Jiang), [taofang@mail.xjtu.edu.cn](mailto:taofang@mail.xjtu.edu.cn) (T. Fang).

<https://doi.org/10.1016/j.apcatb.2019.03.071>

Received 14 January 2019; Received in revised form 21 March 2019; Accepted 27 March 2019

Available online 01 April 2019

0926-3373/ © 2019 Elsevier B.V. All rights reserved.

different kinds of catalysts [15–19]. On the contrary, the dehydrogenation of 12H-NEC is hard to proceed at mild conditions regardless of conversion rate or selectivity. Sotoodeh et al. first reported that 12H-NEC can achieve complete conversion on a 5 wt% Pd/SiO<sub>2</sub> catalyst at 101 kPa and 443 K. However, the selectivity was poor. The product was mixed with not only the complete dehydrogenation product of NEC, but also a large amount of octahydro-*N*-ethylcarbazole (8H-NEC) and tetrahydro-*N*-ethylcarbazole (4H-NEC) intermediates [20]. Cheng et al. did a lot of research on 5 wt% Pd/Al<sub>2</sub>O<sub>3</sub> catalysts and found that the temperature difference of the step-by-step dehydrogenation initiation was large, followed by 401 K, 418 K and 453 K [14,21]. Wesserscheid et al. monitored the adsorption and heat of 12H-NEC on Pd/Al<sub>2</sub>O<sub>3</sub>/NiAl {110} and Pd {111} model catalysts under ultra-high vacuum conditions between 120 K and 520 K. The surface reaction was induced to further elucidate the removal sequence of H in the dehydrogenation [22,23]. Kustov et al. prepared a series of bimetallic Pd-M/TiO<sub>2</sub> (M = Ru, Pt, Cr, Ni, Ge, W) catalysts by a deposition-precipitation procedure, whereas the conversion rate of 75% of 12H-NEC was achieved in thermal mode only by PdRu/TiO<sub>2</sub> and PdPt/TiO<sub>2</sub> for the reaction time about 6 h at 468 K [24]. Amende et al. also investigated the mechanism of dehydrogenation of 12H-NEC on the surface of Pt-based catalysts [25,26]. Jensen et al. also developed a homogeneous Ir-complexation catalyst for the dehydrogenation of 12H-NEC, but there was not formation of NEC detected at 473 K [27]. The best performance bimetallic catalyst was reported from the Pd<sub>2</sub>Ru@SiCN (0.52 mol% active metal) catalyst synthesized by Forberg et al., which can react at 453 K for 7 h with a mass ratio of 1:5 of catalyst to 12H-NEC to reach 5.51 wt% hydrogen release to meet the expected requirements of US DoE [28].

Graphene-loaded noble metals and inexpensive metal catalysts have been extensively studied in many other organic reactions [29–34]. In our previous study, we designed a simple preparation method, and the single metal Pd/rGO catalyst with the highest dehydrogenation activity was obtained by the introduction of reduced graphene oxide (rGO), in which 5.74 wt% hydrogen release and 97.65% selectivity to NEC could be achieved within 7 h at 453 K [35,36]. At the same time, the 2.5 wt% (0.28 mol%) precious metal Pd content was also regarded as the lowest amount of precious metal dosage in the dehydrogenation reaction of 12H-NEC. In fact, we also used bimetallic PdAu/rGO catalysts to improve dehydrogenation efficiency [37]. However, the price of precious metals is still relatively high. If the amount of precious metals can be reduced by some means without causing a decrease in reactivity, the application prospects of such LOHCs will be more competitive. In general, the doping of a second inexpensive metal is the most commonly used strategy for reducing the employment of precious metals. Catalysts made from abundant and inexpensive metals are of great interest because of their potential as viable alternatives to precious metal catalysts used in many chemical reactions [38]. The doping of the second metal often results in unique properties due to its different morphology and structure [39,40]. For the second inexpensive metal doping of Pd-based catalysts, Cu is a common consideration [41–46]. Cu is a 3d transition metal with unique electronic reactivity [47]. Therefore, Cu-based nanocatalysts have been developed in many applications, such as catalytic organic conversion, electrocatalysis and photocatalysis [48–51]. The differences in lattice parameters and atomic radius between Cu and Pd are small, which are beneficial to the formation of a wider range of alloy structures and facilitates the precise regulation of activity and selectivity in catalytic reactions. So far, researchers have prepared a large number of PdCu bimetallic catalysts with different morphologies through various synthetic strategies [41–45]. And also, there are reports for PdCu NPs supported on graphene surface [52–56], but some limitations are still worth improving: First of all, in order to obtain bimetallic PdCu with well-defined morphology, it is often necessary to use a surfactant or a surface active system, which increases the complexity of the post-treatment process, and the particle sizes are usually larger than 10 nm; Secondly, as far as

we know, there is no solution phase synthesis route to achieve a large-scale ratio of PdCu NPs under an approximate particle size distribution for a single factor performance comparison; At last, currently for the dehydrogenation catalyst of the LOHC system, there is no report on PdCu bimetallic catalysts. In fact, for the dehydrogenation of 12H-NEC, there is no related research on any inexpensive second metal doping. The reason is the performance of the previous precious metal catalysts is not satisfactory. Therefore, the design of a bimetallic catalyst applied to 12H-NEC dehydrogenation has become an interesting topic.

In this paper, we have assembled a series ratios of Pd-Cu NPs with a uniform size on the surface of rGO by one-pot method without adding other surfactants, by using the excellent dispersion characteristics of the ethylene glycol-water system found in our previous studies [35,36]. In the catalytic dehydrogenation of 12H-NEC, the obtained PdCu/rGO catalysts continued to reduce the amount of precious metal Pd while maintaining the existing best reaction rate and selectivity of Pd/rGO mentioned above. By simply adjusting the proportion of metal precursors, the components in the catalysts could be well controlled, and a monodisperse catalysts structure could be obtained. The effects of PdCu ratio and synthetic temperature on catalytic activity were systematically compared. Combined with the characterization of the catalysts, the corresponding influence mechanism was explored.

## 2. Experimental section

### 2.1. Materials

*N*-ethylcarbazole (97%), sodium tetrachloropalladate (II) (Na<sub>2</sub>PdCl<sub>4</sub>, 99.9%) and copper (II) chloride dihydrate (CuCl<sub>2</sub>·2H<sub>2</sub>O, 99.9%) were purchased from Aladdin. 5 wt% Ru/Al<sub>2</sub>O<sub>3</sub> catalyst was obtained from Shaanxi Kaida Chemical Engineering Co., Ltd. Sodium citrate dihydrate (AR) and ethylene glycol (AR) were supplied by Sinopharm Chemical Reagent Co., Ltd. Ultra-high purity hydrogen (99.99%) and argon were supplied by Xi'an Tianze gas company. All the chemicals were used as received without any treatment.

### 2.2. Synthesis of Pd<sub>x</sub>Cu<sub>y</sub>/rGO bimetallic catalysts

In a typical synthesis of Pd<sub>1.2</sub>Cu/rGO, GO (0.125 g) (synthesis method in Supporting Information) was dispersed in water (25 mL) and stirred for 2 h. Subsequently, the mixture was treated in an ultrasonic water bath (150 W) for 1 h and then ultrasonic crush (600 W) for 60 min to ensure complete dispersion and peeling of GO. Then 250 mg of sodium citrate was added thereto and stirred well. The mixed solution was transferred to a three-necked flask, and after mixing with 125 mL of ethylene glycol, 0.5 mL of a copper chloride solution (15 mg/mL) and 0.55 mL of a sodium tetrachloropalladate solution (14 mg/mL) were sequentially added, and ultrasonically stirred for 15 min. The reaction mixture was rapidly heated to 393 K with condensation reflux and kept for 5 h. After the reaction was completed, centrifugal washing was carried out with a large amount of water and absolute ethanol until no chloride ions were detected by the AgNO<sub>3</sub> solution. After vacuum drying overnight at 333 K, the powder was ground to 200 mesh, which was designated as product Pd<sub>1.2</sub>Cu/rGO.

Keeping the other conditions unchanged, the samples of Pd<sub>1.2</sub>Cu<sub>0.5</sub>/rGO, Pd<sub>1.2</sub>Cu<sub>2</sub>/rGO, Pd<sub>1.2</sub>Cu<sub>4</sub>/rGO and Pd<sub>1.2</sub>Cu<sub>8</sub>/rGO can be obtained sequentially by changing the added amount of copper chloride solution to 0.25 mL, 1 mL, 2 mL and 4 mL. The samples of Pd<sub>0.6</sub>Cu/rGO and Pd<sub>1.8</sub>Cu/rGO can be obtained by sequentially changing the sodium tetrachloropalladate solution to 0.275 mL and 0.825 mL. Maintaining the amount of sodium tetrachloropalladate and copper chloride solution in Pd<sub>1.2</sub>Cu/rGO unchanged, the samples of Pd<sub>1.2</sub>Cu/rGO-373 and Pd<sub>1.2</sub>Cu/rGO-413 were obtained by changing the reduction temperature to 373 K and 413 K.

### 2.3. Catalyst characterization

X-ray diffraction (XRD) spectra were collected on a Shimadzu LabX XRD-6100 diffractometer at 40 kV and 30 mA with Cu K $\alpha$  radiation ( $\lambda = 1.5406 \text{ \AA}$ ) in the range from  $6^\circ$  to  $90^\circ$ . The laser Raman spectroscopy of the catalysts was carried out on a LabRAM HR Evolution with an excitation wavelength of 532 nm and a scanning range of  $1000 \text{ cm}^{-1}$  to  $2000 \text{ cm}^{-1}$ . X-ray photoelectron spectra (XPS) were recorded on a Thermo Scientific Escalab Xi + system with an X-ray source of monochrome Al K $\alpha$  (1486.6 eV) at 207 W and a  $650\text{-}\mu\text{m}$  beam spot. High-resolution transmission electron microscopy (HRTEM) images were obtained using an accelerating voltage of 200 kV (JEOL JEM-F200).

### 2.4. Preparation of dodecahydro-N-ethylcarbazole

12H-NEC was obtained through the complete hydrogenation of NEC. NEC and commercial Ru/Al $_2$ O $_3$  catalyst with a ratio of 20:1 were loaded into a 250-mL 316 L stainless steel batch reactor (supplied by Anhui Kemi Machinery Technology Co., Ltd.) with magnetic stirring. The reactor was heated to 453 K under the protection of argon. Then, ultra-high purity hydrogen was added to pressurize the reactor to 8 MPa. The reaction was carried out for 4 h under stirring, yielding a gravimetric hydrogen density of 5.79 wt% with a conversion of 100%.

### 2.5. Dehydrogenation of dodecahydro-N-ethylcarbazole

1.5 g of liquid 12H-NEC was loaded in a 10-mL three-necked flask reactor with condensation reflux under magnetic stirring. The solution was heated to 453 K under the purge of argon at 30 mL/min. After the desired temperature was achieved, 0.1 g of the prepared catalysts above was injected into the reactor. Periodically, a very small amount of 8  $\mu\text{L}$  liquid sample was taken out to dilute to a fixed multiple of 10 with decalin for GC-MS (Shimadzu GCMS-QP2010) testing to determine the dehydrogenation extent by quantitative analysis.

## 3. Results and discussion

### 3.1. Characterization of Pd $_x$ Cu $_y$ /rGO bimetallic catalysts

We performed XRD characterization on all prepared catalysts, and

the results are shown in Fig. 1. For convenience of description, we divide the pattern into six 2-theta regions with six different colours,  $8\text{--}20^\circ$  (green),  $20\text{--}32^\circ$  (olive),  $32\text{--}42^\circ$  (red),  $42\text{--}45^\circ$  (orange),  $45\text{--}60^\circ$  (blue) and  $60\text{--}90^\circ$  (purple). In the green region, the main peak should be the sharp Bragg peak of graphite oxide. As shown in Fig. 1, the peak of graphite oxide appears only in the Pd $_{1.2}$ Cu-373 sample reduced at 373 K, but the peak shape also tends to be flat, indicating that under this condition, the oxygen-containing functional group in graphite oxide has begun to partially remove, but the reduction is not thorough. When the reduction temperature is raised to 393 K and 413 K, the GO in the other samples is effectively reduced. At  $23.5^\circ$  of the olive region, it is a typical C (002) peak similar to amorphous diffraction of rGO. This is because GO has been completely exfoliated, so even if a large amount of oxygen-containing functional groups were removed during the reduction treatment, it was impossible to return to the original ordered layered structure like in graphite. The rGO can only be arranged in an unordered manner, with an amorphous or partially ordered structure. The new structural defect that may form during the oxidation process is also one of the reasons for the broadening of the diffraction peak shape. It can be seen that the peaks of rGO appear in all the samples and the peak shape and degree of broadening are similar. Only the peak intensity of Pd $_{0.6}$ Cu is relatively high. The possible reasons are from two aspects: Due to the lowest molar fraction of metal in this sample, the relative intensity change caused by the low intensity of the overall diffraction peak has shown up, and the lower diffraction intensity of other parts in this sample can support this interpretation. Second, the metal Pd may be mainly used as the "anchor element" to the oxygen-containing functional group on rGO surface. The low content of Pd cannot occupy all the adsorption sites, resulting in the characteristic peak of rGO intrinsic can be partially revealed. There are similar phenomena in the references, and not all metals are equally involved in anchoring on rGO surface [37,57,58].

The regions corresponding to the latter four colours only contain the peaks of metals. Firstly, it is shown that PdCl $_4^{2+}$  and Cu $^{2+}$  ions can be effectively reduced to the elemental substance under each condition. In addition, it can be clearly seen that the red region should appear in the fcc Pd {111} facet of  $40.1^\circ$  and the fcc Cu {111} facet of  $43.3^\circ$ . The two sharp metal diffraction peaks expand and widen into one span around  $4^\circ$ , indicating that Pd and Cu form an alloy structure with small particle size and maintain the original fcc structure. At the same time, the

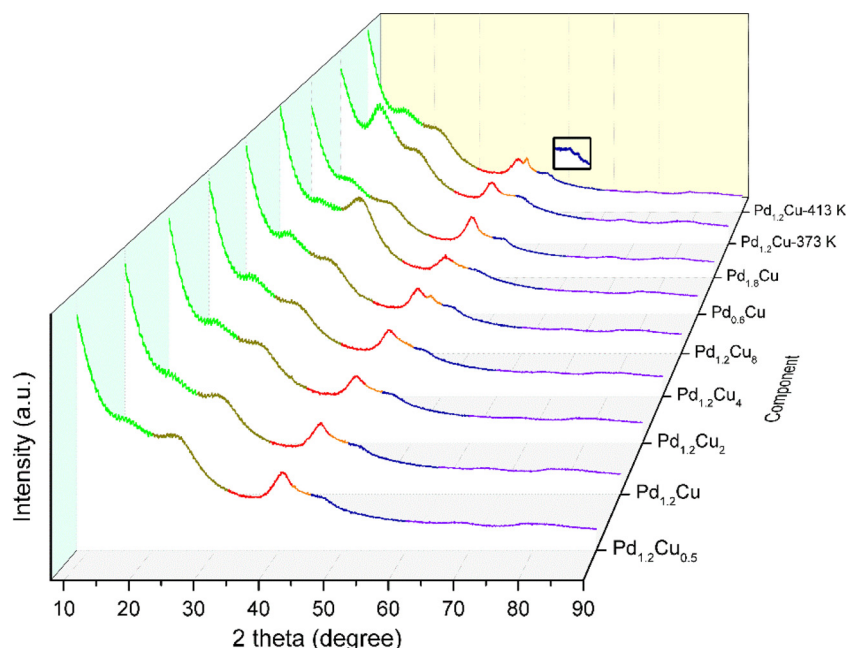


Fig. 1. XRD patterns of catalysts obtained at different PdCu ratios and reduction temperatures. (A 2D image was shown in Fig. S2 in Supporting Information.).

degree of peak broadening in different samples is generally consistent, demonstrating that the particle sizes of PdCu NPs formed at different ratios and temperatures are not that different. This can be further verified in the equally broadened {200} peak region at 47–49° in the blue region. The broadening of such a diffraction peak may also be caused by a polycrystalline alloy structure. With respect to the single crystal structure, the diffraction range of the polycrystalline structure becomes larger due to grain refinement, and the number of superpositions is reduced at the same theta angle, so that the diffraction peak intensity is reduced and the peak is broadened. However, there are two kinds of catalysts which are significantly different from other samples, that is, the orange regions of Pd<sub>1.2</sub>Cu<sub>8</sub> and Pd<sub>1.2</sub>Cu-413 exhibit an additional diffraction peak of Cu {111} facet. For Pd<sub>1.2</sub>Cu<sub>8</sub>, when the amount of Pd is fixed and the amount of Cu is increased from 0.5 to 8, it can be seen that PdCu species maintain the same broadening degree of diffraction peak in the ratio range of 0.5 to 4. When continue increasing Cu to 8, a relatively weak but identifiable diffraction peak of Cu {111} appears, which indicates that not all the PdCu ratios are appropriate to form alloy structure under the preparation conditions. During the crystal growth process, if the proportion of Cu is too high, some Cu atoms cannot be doped into the lattice of Pd or form a surface covering as scheduled, but are aggregated into a core by itself, and then continuously obtain sufficient Cu atoms to form small clusters to reduce the overall surface free energy. This will crystallise a mixed structure in which the bimetallic PdCu coexists with Cu, but the elemental Cu content should not be high because a distinct Cu {200} peak cannot be identified at the broadened {200} peak position. In contrast, Pd<sub>1.2</sub>Cu-413 is another case. Comparing the three different reduction temperatures of the same molar ratio of Pd<sub>1.2</sub>Cu, it can be seen that only when it rises to 413 K, a more pronounced Cu {111} peak appears, and the peak shape is sharper than Pd<sub>1.2</sub>Cu<sub>8</sub>. This indicates that the higher reduction temperature disturbed the doping process of Cu into Pd during the co-reduction process. Crystal growth at higher temperatures is thermodynamically controlled, and Pd and Cu atoms rapidly nucleate in different regions on the rGO surface at the beginning of the reduction, and the relatively elevated reduction rate due to the increase in temperature allows the atoms required for crystal growth to be quickly replenished. Therefore, a cluster of elemental Cu forms, and the content of elemental Cu is even higher than that of Pd<sub>1.2</sub>Cu<sub>8</sub> because two weak diffractions can be observed in Pd<sub>1.2</sub>Cu-413 in the blue {200} diffraction region. The peak, judged from the diffraction angle, should be derived from the bimetallic PdCu and the Cu element, respectively. For the high angle region of 60–90° in purple, since the particle sizes are too small, no obvious diffraction peaks could be observed, and similar phenomena are reported in the references [45,46,52–54].

Fig. 2 shows the TEM images of the morphology and microstructure of the catalysts with the fixed amount of Pd and reduction temperature when the amount of Cu is changed to 0.5, 1 and 4 typically. It can be seen that the samples have similar monodispersity when the amount of Cu changes, even if surfactant was not used in the preparation process, PdCu NPs can be relatively uniformly dispersed on the rGO surface. At the same time, the shape of the nanoparticles is spherical, and the average particle sizes of Pd<sub>1.2</sub>Cu<sub>0.5</sub>, Pd<sub>1.2</sub>Cu and Pd<sub>1.2</sub>Cu<sub>4</sub> are 4.13 nm, 3.80 nm, and 4.11 nm, respectively. The particle size of Pd<sub>1.2</sub>Cu is relatively small but the difference between the samples is not large, with an approximate particle size level. It is worth noting that, from the distribution of particle size, when the amount ratio of Cu is increased to 4, the number of NPs between 4.5 and 6.0 nm in diameter began to increase, and NPs less than 3 nm become rare. This particle size is somewhat different comparing the approximately normal distribution in the other two samples. Obvious lattice spots and fringes can be seen in the HRTEM image with the 5 nm scale bar, indicating that the PdCu NPs have a good degree of crystallization, but there are few cases where the diffraction fringes are only in one direction in a single particle, indicating that the PdCu NPs are mainly in polycrystalline form. It is clearly shown in the HRTEM image inserted in Fig. 2(f) with 2 nm scale

bar, that the lattice spots and fringes have multiple orientations in one particle. This phenomenon can further verify the interpretation of diffraction peak broadening in XRD analysis. In addition, after careful comparison, it is found that as the ratio of Cu increases to 4, the spherical shape of some NPs begins to stretch, resembling a rugby-like shape, and begin to gradually move toward the particle morphology of elemental Cu.

TEM images of the catalysts, when the amount of Cu and the reduction temperature were fixed and the amount of Pd was changed, are shown in Fig. 3. It can be seen that the NPs therein maintain a spherical morphology as in the case of changing the amount of Cu, and a similar polycrystalline structure can also be observed from HRTEM. At the same time, the two have the same normal particle size distribution as Pd<sub>1.2</sub>Cu in Fig. 2. The average particle size of Pd<sub>0.6</sub>Cu is 3.99 nm, and the average particle size of Pd<sub>1.8</sub>Cu is 4.06 nm. The particle sizes are similar to the three catalysts above. In addition, comparing the morphology change in Pd<sub>1.2</sub>Cu<sub>4</sub> by adding Cu, we can also know that the various amount of Pd has little effect on the morphology of NPs, which may be because the nanoparticles of Pd are themselves spherical. Moreover, the particle size of elemental Pd NPs prepared in our previous study by a similar dispersion method was 3.27 nm, [35] and the introduction of Cu brought about a particle size growth of about 0.8 nm. At this point, one of the problems mentioned in our introduction can be solved. In the solution phase synthesis route, we have realized the ratio of PdCu regulation under the approximate particle size distribution, and have proved the advantages and specificity of this catalyst preparation method.

The TEM images of the morphology and microstructure of Pd<sub>1.2</sub>Cu NPs at different reduction temperatures are shown in Fig. 4. NPs are still monodispersed sphere in the TEM image, with average particle sizes of 4.40 nm (373 K) and 4.26 nm (413 K), respectively. Combined with an average particle diameter of 3.80 nm at 393 K in Fig. 2, the temperature has a large effect on the same proportion of PdCu NPs and the effect is not linear, owing to the product components at different temperatures are diverse. From the analysis of XRD, we have known that at the reduction temperatures of 373 K and 393 K, the product is the polycrystalline alloy structure of PdCu, and elemental Cu appeared after the reduction temperature was raised to 413 K a polycrystalline copper nanoparticle is shown in Fig. 4(f). The lattice distance of 0.209 nm shows that it is a typical Cu {111} facet, validating the XRD analysis.

The differences between metal NPs can be explained intuitively in TEM analysis, but the description of supporter rGO is weak. Therefore, Raman spectroscopy is needed to identify the microstructure effects of rGO at different ratios and reduction temperatures. A comparison of the Raman spectra of the different catalysts is shown in Fig. 5. It can be seen that, unlike GO, all catalyst samples have a relatively high intensity of D band (1350 cm<sup>-1</sup>), which is resulted from the lattice vibration deviating from Brillouin zone center, [59] meaning that the original two-dimensional planar structure was destroyed during the deep oxidation process, and a portion of C in sp<sup>2</sup> hybridized six-membered ring was transformed into sp<sup>3</sup> hybridized C to form planar defects or bond with the O atom, resulting in the degree of disorder increasing dramatically. The other characteristic peak is the G band caused by the stretching vibration of sp<sup>2</sup> hybridized C atoms in the plane at 1592 cm<sup>-1</sup>, which is capable of showing the number of layers of graphene sheets and is highly susceptible to stress and doping [60]. Comparing the D and G band positions of different catalysts, it can be found that the metal loading and the reduction temperature of different ratios do not cause a significant red shift or blue shift of the D and G band, so we can conclude that in the same reduction system, the condition changes within a certain range will not make the rGO itself reflect significant differences. However, comparing the data in our previous study of Pd/rGO, [35] it is found that the addition of Cu resulted in a blue shift of 4 wave-numbers in the G band of all samples relative to the G band of Pd/rGO (1588 cm<sup>-1</sup>, Fig. S3 in Supporting Information), indicating that the

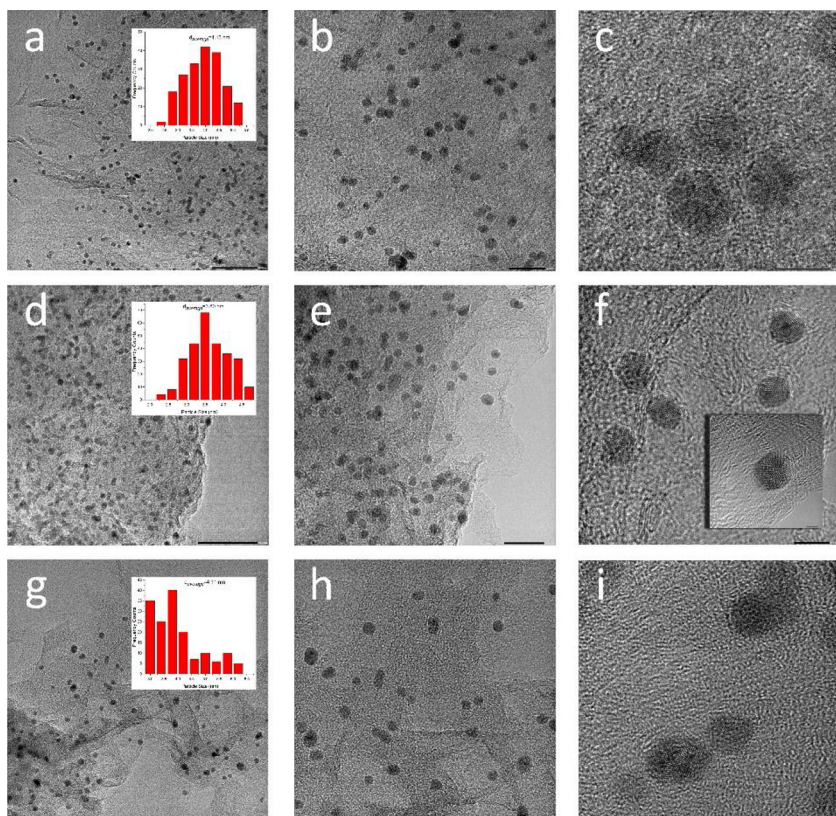


**Fig. 2.** TEM images of (a–c)  $\text{Pd}_{1.2}\text{Cu}_{0.5}/\text{rGO}$ , (d–f)  $\text{Pd}_{1.2}\text{Cu}/\text{rGO}$  and (g–i)  $\text{Pd}_{1.2}\text{Cu}_4/\text{rGO}$ . The inserted images in a, d, and g are the particle size distribution of the corresponding samples, and the inserted image in f is HRTEM image with a 2 nm scale bar. The image scale bar in the same row is 50 nm, 20 nm and 5 nm from left to right.

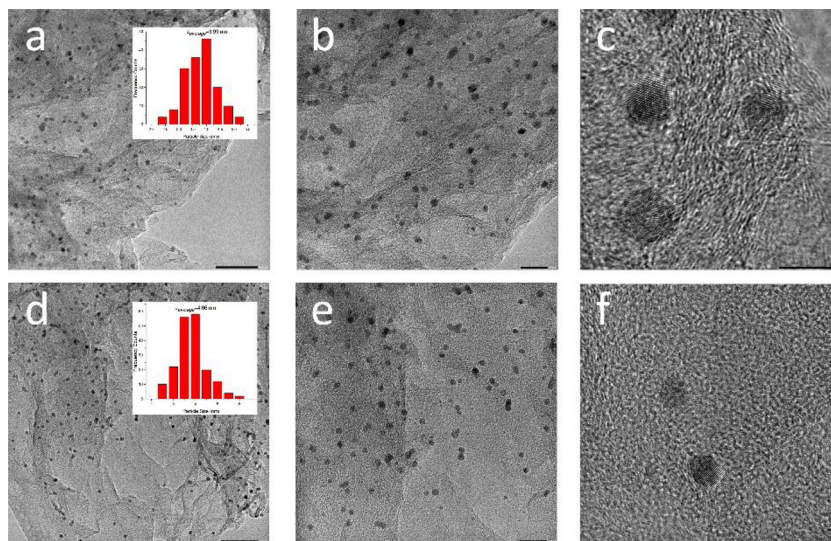


**Fig. 3.** TEM images of (a–c)  $\text{Pd}_{0.6}\text{Cu}/\text{rGO}$  and (d–f)  $\text{Pd}_{1.8}\text{Cu}/\text{rGO}$ . The inserted images in a and d are the particle size distribution of the corresponding samples. The image scale bar in the same row is 50 nm, 20 nm and 5 nm from left to right.

Raman scattering fluctuation in the two-dimensional plane became shorter, the vibration became stronger, and the electrons are activated relative to the elemental Pd.

The figure in the upper right corner of Fig. 5 is a plot of the ratio of  $I_D/I_G$  (D band intensity/G band intensity) in different catalysts, which can be used to identify the relative degree of disorder of different catalyst structures. Since the reduction system is a glycol/water and sodium citrate system, the  $I_D/I_G$  ratio of the different catalysts is in a relatively narrow range, and the most significant factor is the reduction temperature. In the XRD analysis, we have found that GO is not fully reduced to rGO during the reduction at 373 K, which can also be verified from its smallest  $I_D/I_G$  ratio. When the temperature rises to 393 K,

the  $I_D/I_G$  ratios of each sample fluctuate within a narrower box interval. After continuing to rise the temperature to 413 K, the higher temperature increases the ability of the reduction system, making the oxygen-containing functional group relatively more effective to remove and bring more planar defects, so  $\text{Pd}_{1.2}\text{Cu}$ -413 K is with the largest  $I_D/I_G$  ratio. In addition, in the catalysts reduced at 393 K,  $\text{Pd}_{0.6}\text{Cu}$  is relatively far from the ratio fluctuation range of other samples. The possible reason and the analysis in XRD can be mutually verified. Because  $\text{Pd}_{0.6}\text{Cu}$  is with the lowest mole fraction of metal, the most of Pd and part of Cu are involved in the anchoring to the surface of rGO, thus making the oxygen-containing functional group which can be used for adsorption in an idle state. It makes the supporter closer to the state of

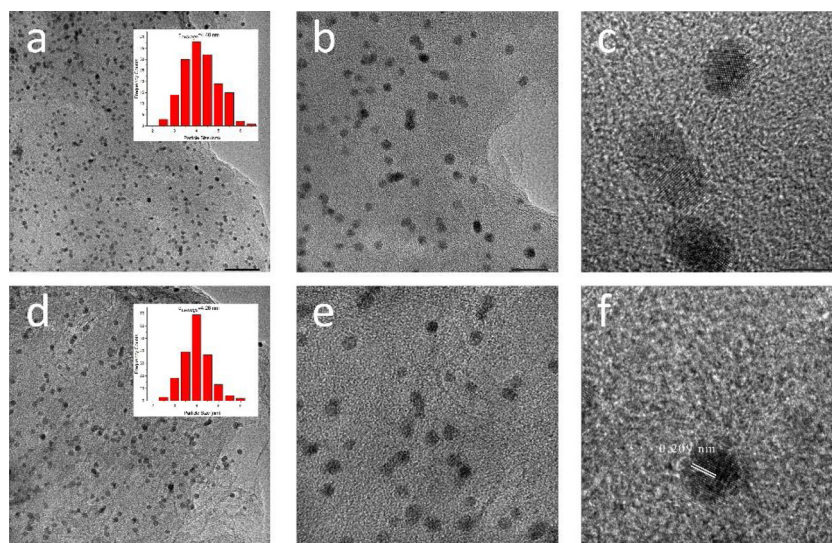


**Fig. 4.** TEM images of (a–c)  $\text{Pd}_{1.2}\text{Cu}/\text{rGO}-373$  and (d–f)  $\text{Pd}_{1.2}\text{Cu}/\text{rGO}-413$ . The inserted images in a and d are the particle size distribution of the corresponding samples. The image scale bar in the same row is 50 nm, 20 nm and 5 nm from left to right.

original GO, and thus the  $I_D/I_G$  ratio is smaller compared with other samples, but still larger than  $\text{Pd}_{1.2}\text{Cu}-373$  K.

Detailed information on the distribution of elements and valence states in different catalysts can be obtained by further XPS analysis. Because the preparation conditions of different catalysts are almost the same, the peak shape and distribution in XPS fitting are very similar. The representative peak fittings are listed in Fig. 6, and the elemental analysis data is summarized in Table 1. Fig. 6(a) is the C1s spectrum of  $\text{Pd}_{1.2}\text{Cu}/\text{rGO}$ , and there are four different bonding forms of C element [61]. In the analysis above, we have already known that the difference in rGO is not obvious, so the C1s fitting of each sample only differs in

the proportion of the four bonding forms, while the peak type is consistent. It can be more clearly seen from the distribution of the C element in Table 1 that the content of carbonyl C and carboxyl C is almost the same in the reduction process of GO in different samples, indicating that the deep oxidized oxygen-containing group cannot be reduced under the conditions of this system. At the same time, consistent with the XRD and Raman analysis results, the differences caused by the reduction temperature can also be more obvious. At 373 K, the C–C bond content is the lowest, and some of the easily reduced C–O bonds are not removed completely. When the temperature is raised to 393 K, this part of the C–O bond is reduced to C–C bond, so the corresponding content

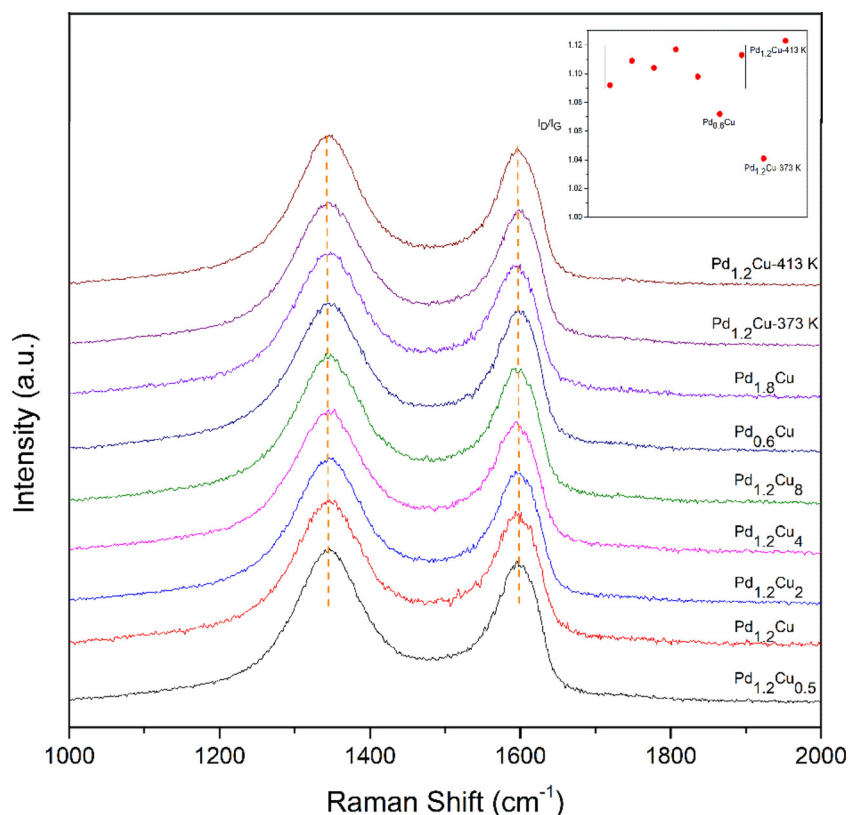


**Fig. 5.** Raman spectra of different catalysts, the picture inserted in the upper right corner is the ratio distribution of  $I_D/I_G$ .

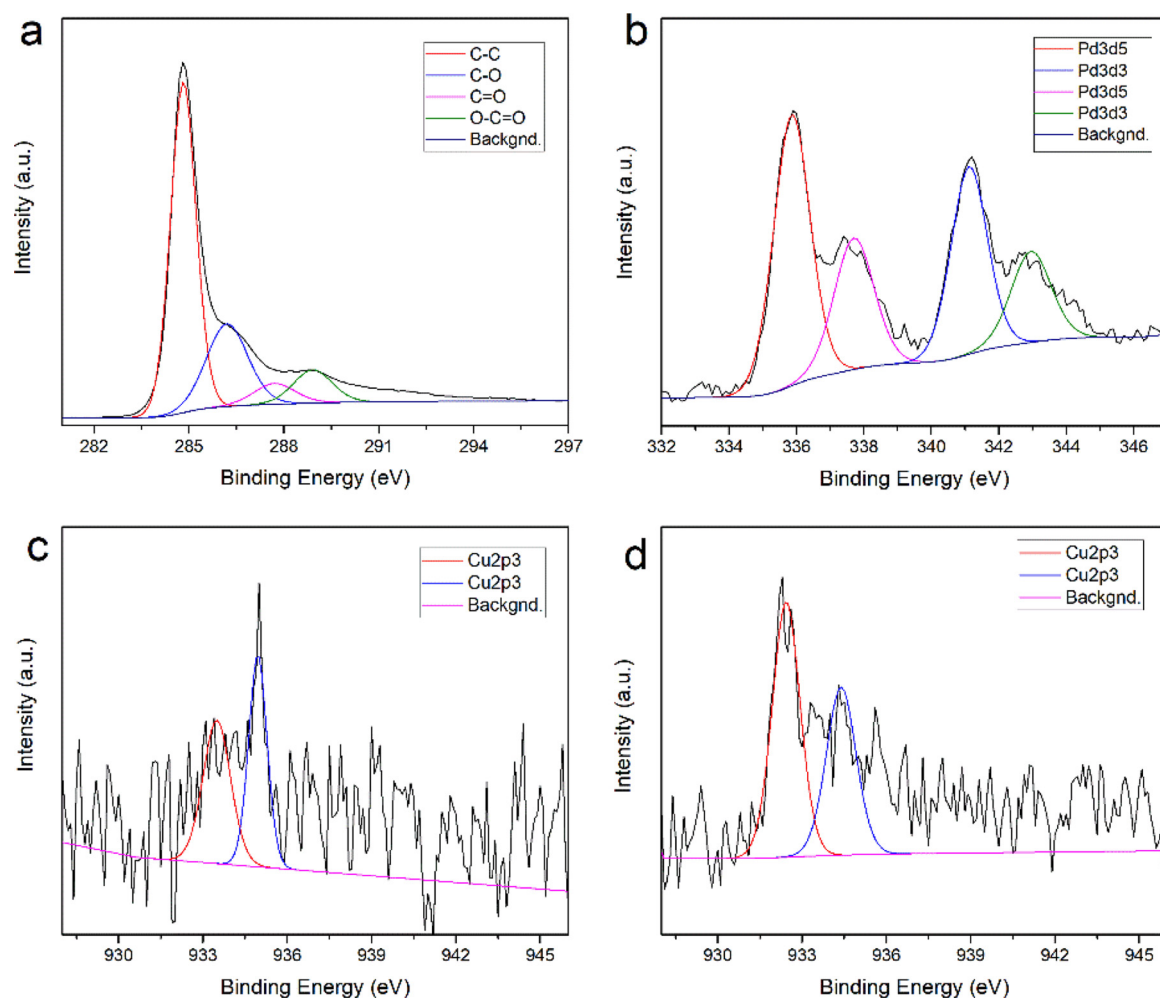


Fig. 6. XPS peak fitting of typical samples, C1s of (a)  $\text{Pd}_{1.2}\text{Cu}/\text{rGO}$ , Pd 3d of (b)  $\text{Pd}_{1.2}\text{Cu}/\text{rGO}$ , Cu 2p of (c)  $\text{Pd}_{1.2}\text{Cu}/\text{rGO}-373$  and (d)  $\text{Pd}_{1.2}\text{Cu}/\text{rGO}-413$ .

changed. Regardless of the ratio of the active component, there is no significant influence on the rGO component at this temperature, indicating that the reduction of GO in the unified system is mainly determined by temperature. When continue rising the temperature to 413 K, in addition to the C–O bond, the carbonyl group which is easily removed inside the two-dimensional plane begins to participate in the reduction, and an obvious content is reduced. The planar edge carboxyl group with the highest degree of oxidation cannot be effectively reduced in this system [62].

Similar to the C element, Pd also maintains a peak shape consistent in each sample, and only the difference in valence distribution exists, so the Pd 3d spectrum peak fitting of  $\text{Pd}_{1.2}\text{Cu}/\text{rGO}$  is still used as a representative. A set of double peaks at 335.9 eV and 341.2 eV correspond

to the  $\text{Pd}3d_{5/2}$  and  $\text{Pd}3d_{3/2}$  of the elemental Pd, respectively, while a set of weak double peaks at 338.5 eV and 343.6 eV correspond to the oxidized valence form of palladium ( $\text{Pd}^{8+}$ ). It has been demonstrated in previous studies that since there was no  $\text{PdO}_x$  species in the XRD analysis, the oxidation state of  $\text{Pd}^{8+}$  present here is an electron shift caused by adsorption bonding with the oxygen functional group on the rGO surface [35–37]. Unlike the C element, the valence distribution of Pd is more affected by the temperature and molar ratio of PdCu. Comparing the distribution of Pd in  $\text{Pd}_{1.2}\text{Cu}$  at three temperatures, it can be seen that the proportion of elemental Pd at 373 K is only 50.31%, which is due to the incomplete removal of oxygen-containing functional groups at low temperature, and Pd can be adsorbed with more O atoms. After the temperature is increased by 20 K, the content of Pd is also increased

Table 1

XPS elemental analysis of different catalysts.

Sample name	Atomic percentage (%)				Mole fraction (%)					
	C–C	C–O	C=O	O–C=O	Pd	$\text{Pd}^{8+}$	C	O	Pd	Cu
$\text{Pd}_{1.2}\text{Cu}_{0.5}/\text{rGO}$	60.40	24.52	5.46	9.62	58.84	41.16	80.45	19.22	0.22	0.11
$\text{Pd}_{1.2}\text{Cu}/\text{rGO}$	60.07	24.68	5.85	9.40	61.54	38.46	78.96	20.61	0.23	0.20
$\text{Pd}_{1.2}\text{Cu}_2/\text{rGO}$	59.98	24.90	5.97	9.15	63.31	36.69	78.95	20.46	0.22	0.37
$\text{Pd}_{1.2}\text{Cu}_4/\text{rGO}$	59.72	25.03	5.74	9.51	63.34	36.66	77.89	21.09	0.21	0.81
$\text{Pd}_{1.2}\text{Cu}_8/\text{rGO}$	59.43	25.15	5.83	9.59	63.23	36.77	78.38	20.26	0.19	1.17
$\text{Pd}_{0.6}\text{Cu}/\text{rGO}$	59.31	25.83	5.41	9.45	48.24	51.76	78.56	20.87	0.16	0.41
$\text{Pd}_{1.8}\text{Cu}/\text{rGO}$	59.54	24.86	5.86	9.74	62.85	37.15	78.92	20.50	0.35	0.23
$\text{Pd}_{1.2}\text{Cu}/\text{rGO}-373$	58.41	26.44	5.98	9.17	50.31	49.69	78.36	21.23	0.23	0.18
$\text{Pd}_{1.2}\text{Cu}/\text{rGO}-413$	62.90	23.92	4.02	9.16	64.41	35.59	79.61	19.92	0.25	0.22

to 61.54% due to the removal of C–O bond. After the further increase of 20 K, the elevating of Pd is less than 3%, indicating that the adsorption sites are basically occupied and saturated. At the same temperature and the amount of Cu remaining unchanged, the amount of Pd is increased from 0.6 to 1.2, and the amount of elemental Pd is increased from 48.24% to 61.54%. While the amount of Pd is fixed, in the process of increasing the ratio of Cu from 0.5 to 8, the changing amount of elemental Pd is less than 3%, which confirms the difference between the two metals participating in the anchoring process on rGO surface. The amount of Pd involved in anchoring is relatively high. This can be understood from the viewpoint of redox potential. Compared with the standard hydrogen electrode, the electrode potential of  $\text{PdCl}_4^{2-}$  reduced to elemental Pd is 0.62 V,  $\text{Cu}^{2+}/\text{Cu}$  is 0.34 V. At the beginning of the reaction, some  $\text{Pd}^0$  atoms are first reduced to occupy the adsorption sites. Then, nucleation growth is carried out centering on them. At the same time, the large change of Cu content leading to the small difference of Pd distribution can be explained from the side that Cu is mainly present in the bulk phase or used as surface coverage in NPs. Different Cu content will have a great influence on the coverage. In addition, it can be seen from the molar ratio of Pd and Cu that the prepared catalysts have little difference from the initial feeding ratio, and the ratio error is within 10%.

Fig. 6(c) and (d) are XPS fitting of Cu2p at different temperatures. Cu is relatively active with respect to Pd, so the reduction of Cu in this relatively weak reduction preparation system will be greatly affected by temperature. The two peaks at 932 eV and 935 eV correspond to the  $2p_{3/2}$  of  $\text{Cu}^0$  and  $\text{Cu}^{2+}$ , respectively, and no significant  $\text{Cu}^{2+}$  satellite peaks are observed between 938 and 945 eV [63]. Since the relative content of Cu in each sample is very low, no significant Auger electron spectrum Cu LMM could be collected to determine whether there is  $\text{Cu}^+$  in the peak at 932 eV [64]. In the XRD analysis, we can see that the samples are not mixed with obvious  $\text{CuO}$ ,  $\text{Cu}_2\text{O}$  and  $\text{Cu}(\text{OH})_2$  species, so the  $\text{Cu}^{2+}$  species here we think there are mainly two sources. One is the same as the  $\text{PdO}_x$  species, which is the adsorption with oxygen-containing functional groups on the surface of rGO. And second it's due to the characteristics of Cu NPs themselves, that is, the surface oxidation caused by the excessive sensitivity of nanosized Cu to oxygen and water in the air [40]. It can be seen that the temperature has a great influence on the distribution of Cu species. The content of  $\text{Cu}^{2+}$  is dominant at lower temperature, and it will gradually reverse after increasing the temperature.

### 3.2. Catalytic dehydrogenation study of $\text{Pd}_x\text{Cu}_y/\text{rGO}$ bimetallic catalysts

Fig. 7 is a comparison of the dehydrogenation efficiency at 453 K over time for different ratios of bimetallic  $\text{PdCu}/\text{rGO}$  catalysts. The more detailed comparisons are shown in Fig. 7(b–d). After the NEC was completely hydrogenated to 12H-NEC, the dehydrogenation reaction can release a total of 5.79 wt% of hydrogen. The catalyst represented by  $\text{Pd}_{2.2}$  in the figure is the  $\text{Pd}/\text{rGO}$  catalyst with the highest dehydrogenation activity selected in previous report [35,36]. In general, changing the  $\text{PdCu}$  ratio and the preparation temperature will bring significant effects on the performance of the catalysts. And it can be seen that some catalysts can maintain the original catalytic activity and selectivity after the amount of Pd is reduced by 20–25%, which will be analyzed one by one. It is shown in Fig. 7(b) that when the amount of Pd is fixed at 1.2, the effect of changing the amount of Cu in the range of 0.5–8 is not linear, and only  $\text{Pd}_{1.2}\text{Cu}$  can maintain the NEC selectivity (slightly more than 2%) consistent with  $\text{Pd}_{2.2}$ , even the initial reaction rate is slightly improved.  $\text{Pd}_{1.2}\text{Cu}_{0.5}$  has an approximate dehydrogenation efficiency in the initial 2 h of the reaction, but it cannot be maintained with the extension of the reaction time, and the selectivity decreases slightly.  $\text{Pd}_{1.2}\text{Cu}_4$  is also close to the amount of hydrogen release, but the initial reaction rate of the catalyst is not fast enough. The two catalysts with similar decrease in hydrogen release are  $\text{Pd}_{1.2}\text{Cu}_2$  and  $\text{Pd}_{1.2}\text{Cu}_8$ , which also have relatively close

dehydrogenation reaction rate.

The amount of Cu added in  $\text{Pd}_{1.2}\text{Cu}$  with the highest dehydrogenation efficiency is fixed, and the slightly changed Pd content also has a significant effect, as shown in Fig. 7(c). When the content of Pd is reduced by half to 0.6, the dehydrogenation efficiency is greatly reduced. Although the conversion of 12H-NEC to 8H-NEC and further dehydrogenation to 4H-NEC are relatively easy, the decrease of Pd still greatly reduces the efficiency of this process. While increasing the Pd content by 50% to 1.8, it does not bring about such a significant increase in activity, and the selectivity of NEC is also close to 100% after 7 h of reaction. Further comparison reveals that the increase in the amount of Pd is mainly caused the change in the initial rate of dehydrogenation. In fact, in the first 30 min of the reaction, the increase in Pd reduces the hydrogen release efficiency at this stage. During the 2.5 wt% hydrogen release interval between 30 min and 3 h, the sequence is reversed and after 3 h, both are at the same rate of hydrogen evolution until the reaction is terminated. Taking economic factor into consideration,  $\text{Pd}_{1.2}\text{Cu}/\text{rGO}$  is still the most cost-effective catalyst among all samples, and its dosage of Pd is continuing to decrease by about 20% (0.23 mol% vs 0.28 mol%, or 1.86 wt% vs 2.5 wt%) comparing to  $\text{Pd}/\text{rGO}$  catalyst with consistent dehydrogenation efficiency and selectivity to NEC, and even the initial dehydrogenation rate increases slightly.

As shown in Fig. 7(d), changing the reduction temperature when  $\text{PdCu}$  ratio is fixed brings a more identifiable performance gap. When the reduction temperature is lowered to 373 K, only 2 wt% of stored hydrogen can be released after 7 h. When the reduction temperature is increased to 413 K, the amount of hydrogen released increases, but just exceeds 3 wt%. Only the reduction temperature of 393 K leads to an optimum amount of dehydrogenation. Combined with the catalyst characterization above, we can speculate that the reason for this large difference in catalytic performance is that the reduction temperature changed the composition of the three catalysts: at 373 K, the reduction of graphene oxide was insufficient, and the excess oxygen-containing functional groups caused the near 50% content of  $\text{Pd}\delta^+$ , which limited the activity of Pd and the surface migration of electrons in the two-dimensional plane. After the temperature reached to 413 K, the growth mode of active metal had undergone a great change. Cu did not form a good alloy structure with Pd as well as 393 K, and a large cluster of Cu appeared, which would affect the overall catalytic performance. Therefore, the regulation of the reduction temperature is the key to obtaining a high performance  $\text{PdCu}$  bimetallic catalyst.

In fact, the influence of bimetal on the activity of the catalyst is very significant, but the mechanism is not uniformly explained. Because of the doping type and influencing factors of bimetal varied in different catalysts, it is difficult to carry out single factor correlation analysis in a strict sense. Therefore, for the catalytic dehydrogenation reaction we are facing, we will try to explore from multiple aspects. An important factor affecting the activity of conventional catalysts is the particle size and distribution of the catalytically active components. From the TEM analysis, we can find that the catalysts with different  $\text{PdCu}$  ratios obtained under the preparation system have monodisperse distribution characteristics with no agglomeration being observed. At the same time, regardless of the influence of temperature, the particle size of polycrystalline NPs of each catalyst synthesized at 393 K fluctuates within the range of  $4.1 \pm 0.1$  nm, while the average particle size of  $\text{Pd}_{1.2}\text{Cu}$  with the best catalytic activity is the smallest, identified as 3.80 nm. Smaller particle size is a key factor in its higher reactivity, which has been reported in a number of similar conclusions in previous studies [65,66].

In Raman and XPS analysis of rGO supporter, we verified the similarity of rGO in different catalysts synthesized at 393 K, which can be considered to the same promotion to the bimetallic  $\text{PdCu}$  active components. However, there are significant differences in  $\text{PdCu}$  NPs with different ratios. The XPS measurement data for different ratios of  $\text{PdCu}$  catalysts are shown in Fig. 8(a), with the auxiliary line being the

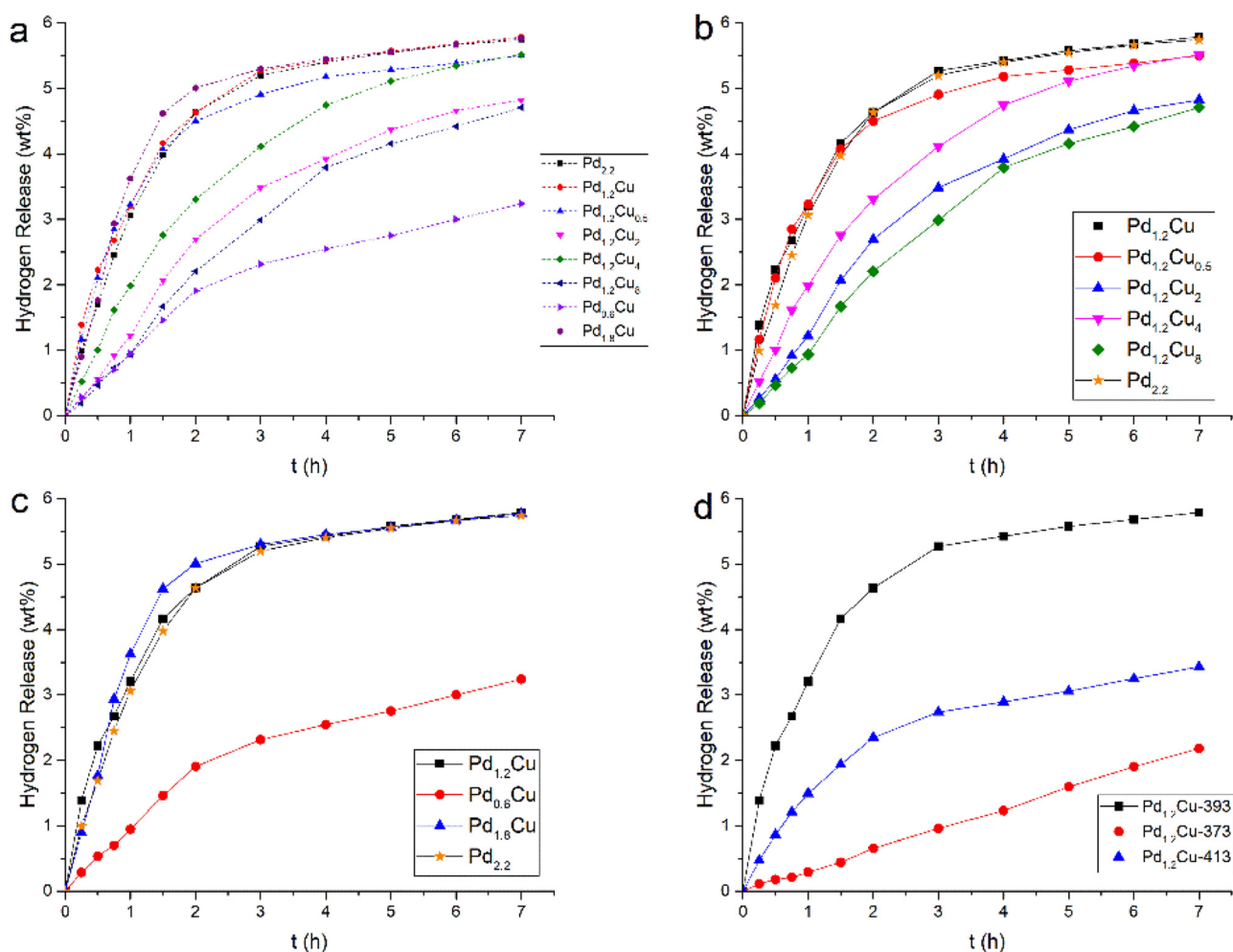


Fig. 7. Dehydrogenation efficiency of different catalysts at 453 K over time, (a) global comparison, (b) specific performance comparison by the changing amount of Cu, (c) specific performance comparison by changing the amount of Pd, (d) specific performance comparison by changing reduction temperature in the co-reduction process.

standard core-level binding energy of  $\text{Pd}3d_{5/2}$  of 335.9 eV. Obviously, as the content of Cu changes, the binding energy of  $\text{Pd}3d$  in the elemental Pd is significantly shifted, which means that the interaction between Cu and Pd is strong and the atomic group effect is evident in  $\text{PdCu}$  NPs. When the proportion of Cu increases from 0 to 50%, virtually no significant change (less than 0.1 eV) can be recognized in the binding energy of  $\text{Pd}3d$ , and the similar binding energy is remained as

in pure Pd. When the Cu content is continuously increased to 86.9% ( $\text{Pd}_{1,2}\text{Cu}_8$ ), the binding energy of  $\text{Pd}3d$  is significantly positively shifted up to about 0.4 eV. This indicates that the  $\text{PdCu}$  NPs should have two different electronic structures before and after the doping amount of Cu reaching 50%. The continuously shift of the binding energy lower than the ratio of 1.2:1 indicates that when the doping of Cu reaches a certain amount, it interferes with the original Pd-Pd bond interaction, and the

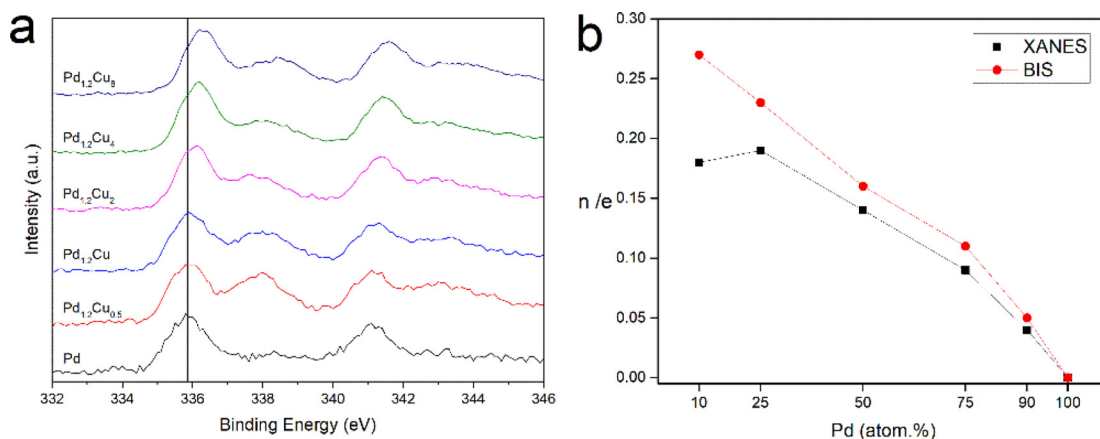


Fig. 8. (a) XPS spectra of core-level binding energy of  $\text{Pd}3d$  in different catalysts by changing the amount of Cu, (b) The amount of electron transfer drawn from the data in the Ref. [61].

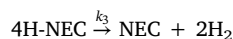
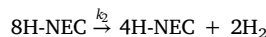
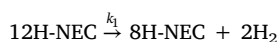
**Table 2**  
Kinetics fitting results of different catalysts at 453K.

Sample	Rate constant $k_1$ , min <sup>-1</sup>	Rate constant $k_2$ , min <sup>-1</sup>	Rate constant $k_3$ , min <sup>-1</sup>	R <sup>2</sup>	H <sub>2</sub> release after 7 h (wt%)	Selectivity for NEC (%)
Pd <sub>1.2</sub> Cu/rGO	0.05509	0.02637	0.00919	0.9974	5.79	100
Pd <sub>1.2</sub> Cu <sub>0.5</sub> /rGO	0.04515	0.02927	0.00611	0.9975	5.50	85.15
Pd <sub>1.2</sub> Cu <sub>2</sub> /rGO	0.01434	0.01065	0.00247	0.9943	4.82	50.50
Pd <sub>1.2</sub> Cu <sub>4</sub> /rGO	0.02460	0.01344	0.00544	0.9952	5.52	86.02
Pd <sub>1.2</sub> Cu <sub>8</sub> /rGO	0.01292	0.00747	0.00233	0.9914	4.71	44.12
Pd <sub>0.6</sub> Cu/rGO	0.01182	0.00240	0.00035	0.9973	3.24	6.83
Pd <sub>1.8</sub> Cu/rGO	0.04401	0.03639	0.01063	0.9955	5.77	99.14

electrons of Pd atoms begin to shift outward to Cu. From the shift direction of binding energy, we judge that the surface of Pd is with a positive charge and the surface of Cu is with a negative charge. From this point of view, we can analyze the sample of Pd<sub>1.2</sub>Cu with the maintaining high activity of Pd/rGO. At this stage, the binding energy of Pd-Pd is not changed by the doping of Cu, but it remains consistent with pure Pd, while the content of Pd is significant reduced due to the doping of Cu. When the amount ratio of Cu starts to rise to 2, 4 or 8, the Pd in the sample begins to lose electrons which will transfer to Cu, and this also explains the sudden drop in performance after the ratio is raised to 2 that it leads to a decrease in dehydrogenation activity requiring electron donation. In the basic research of Lee and coworkers for different proportions of PdCu NPs, similar conclusions were obtained using the more accurate XAS (Pd *L*<sub>III</sub> x-ray absorption spectroscopy) and BIS (bremsstrahlung isochromat spectroscopy) characterization [67,68]. Combined with the core-level binding energy and the theory of energy displacement, [69] they also calculated the specific value of the total charge transfer between Pd and Cu, we draw it into a line in order, as shown in Fig. 8(b). It can be seen that as the Pd content decreases, the amount of charge transferred from Pd will gradually increase. In our characterization, when the content of Cu is between 0 and 50%, the electron transfer does not bring about a significant change in the binding energy, so we can further infer that the outer layer *s* and *d* electrons on the surface of Pd may be redistributed in this region to maintain the overall shielding effect of the outer layer of electrons in Pd to keep the binding energy. Favorable evidence has also been observed by Cho et al. that the unoccupied density of *d* states projected onto the Pd atomic sphere is reduced upon alloy formation with Cu even charge transfer happened from Pd to Cu [68]. This may be the reason for the difference in catalytic activity in those ratios.

### 3.3. Reaction kinetics study

After discussing the mechanism of dehydrogenation performance, we continue to carry out the dehydrogenation reaction kinetics analysis of the prepared catalysts. Fig. 7(a) shows the difference in hydrogen evolution efficiency of the catalysts at 453 K and the specific product distribution is shown in Fig. S4 (see Supporting Information). It can be seen from the product distribution that even in the catalyst with the worst dehydrogenation efficiency, 12H-NEC will be quickly consumed after the start of the reaction, and the conversion rate can reach 100%, further indicating that the first dehydrogenation step is highly prone to occur. Except for Pd<sub>0.6</sub>Cu/rGO with the lowest Pd content, other catalysts can complete the dehydrogenation of 8H-NEC to obtain 4H-NEC before the reaction time is cut off. The conversion of 4H-NEC to the final dehydrogenation product, NEC, is the rate-limiting step of the overall reaction. Combined with the previous research, the influence of internal and external diffusion can be neglected in the kinetic calculation of the reaction, and the whole solid-liquid heterogeneous catalytic reaction can be simplified into the following three elementary reactions [14]:



Where  $k_1$ ,  $k_2$  and  $k_3$  represent the rate constants of the three elementary reactions, and their values can be calculated from the product distribution by our previously designed fitting method [35–37]. Due to the poor activity of the previous dehydrogenation catalyst, the selectivity of the final product NEC was low, so many simplifications were made in the kinetics calculation [20]. Here, the accurate kinetics parameters need to be obtained by solving the numerical solution of the corresponding ordinary differential equations. The algorithm for solving the numerical solution of the differential equation is set to the Runge-Kutta-Fehlberg method, and then the general global optimization is performed. The convergence tolerance is strictly limited to  $1 \times 10^{-14}$ . The fitting results are shown in Table 2.

Obviously, the fitted reaction rate constants can more clearly verify that the NEC formation reaction is the rate-limiting step of the entire dehydrogenation process, which is consistent with experimental observations. The consumption of 12H-NEC has a high rate constant, so all catalysts can complete this process in the dehydrogenation reaction. In addition, except for Pd<sub>0.6</sub>Cu, complete conversion of 8H-NEC can be observed in the product distribution. It can also be judged from the extremely low  $k_2$  of Pd<sub>0.6</sub>Cu. In the activity evaluation, we find that the reaction rate of Pd<sub>1.2</sub>Cu in the first dehydrogenation step exceeds Pd<sub>1.8</sub>Cu, and it gets reversed in the second stage, which can also be confirmed from the relative magnitude of the rate constant. The graphical trend of the rate constants is more intuitive, as shown in Fig. 9. The roughly trend of the rate constants can further verify the relative dehydrogenation efficiency in Fig. 7 and product distribution in Fig. S4. As mentioned above, regardless of the amount of Pd or Cu, the effect on the catalytic activity is not linear, and even the effect on each elementary reaction is not consistent, such as the relative trend of  $k_1$  and  $k_2$  in Pd<sub>1.2</sub>Cu<sub>0.5</sub> and Pd<sub>1.2</sub>Cu, Pd<sub>1.2</sub>Cu and Pd<sub>1.8</sub>Cu. In general, the extreme points of the rate constant curve are basically on Pd<sub>1.2</sub>Cu, and the

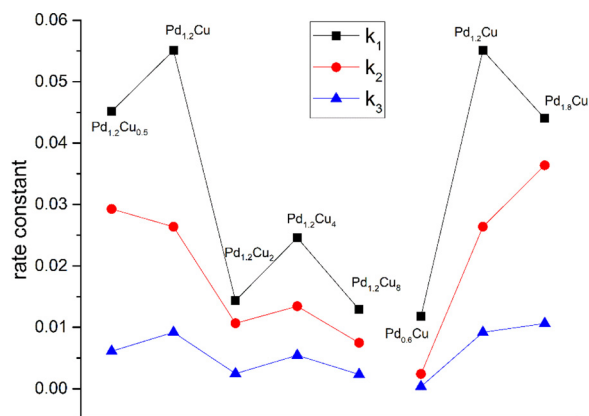


**Fig. 9.** A comparison of the rate constants for the three elementary reactions. The left side is the changing amount of Cu with fixed amount of Pd; the right side is the changing amount of Pd with fixed amount of Cu.

comprehensive consideration of Pd<sub>1.2</sub>Cu/rGO is the most cost-effective bimetallic PdCu ratio.

#### 4. Conclusion

In summary, a series of bimetallic PdCu catalysts with different ratios supported on reduced graphene oxide were prepared by a facile one-pot synthesis method. The most cost-effective Pd<sub>1.2</sub>Cu/rGO catalyst with the lowest amount of precious metals in the catalysts reported for dehydrogenation of dodecahydro-*N*-ethylcarbazole was selected from a series of samples, while maintaining the catalytic activity and selectivity to the final product of *N*-ethylcarbazole as the Pd/rGO catalyst with the highest activity in recently reported studies. To be specific, after 1 h of reaction, the conversion of dodecahydro-*N*-ethylcarbazole reached 100%, and after 7 h of reaction, the selectivity of the final product *N*-ethylcarbazole reached 100% at 453 K. It is capable of completely releasing the stored hydrogen in dodecahydro-*N*-ethylcarbazole, slightly exceeding Pd/rGO, and is equivalent to the reaction rate of Pd/rGO, which is the catalytic activity when the amount of Pd in the precious metal is reduced by 20% to 1.86 wt%. Such a catalyst design will reduce the cost of the catalyst by reducing the amount of precious metal. At the same time, we studied the change of Pd and Cu content and the effect of preparation temperature on dehydrogenation performance, and revealed the variation of reaction kinetics. In combination with various characterization methods of catalyst, we tried to explain the relationship between structure and properties of PdCu NPs in depth. First, the average particle size of Pd<sub>1.2</sub>Cu is the smallest of only 3.80 nm. The smaller particle size is one of the keys to its higher reactivity. Secondly, the electronic structure of PdCu NPs with different ratios is different. When the content of Cu is increased from 0 to 50%, the binding energy of Pd3d does not change significantly, and the characteristics of pure Pd are maintained. When the amount of Cu continues to increase, electron transfer from Pd to Cu begins to occur, which leads to a decrease in dehydrogenation activity requiring electron donation. At the same time, the PdCu ratio will also bring about the redistribution of the outer electrons of Pd, which is another key factor affecting the catalytic activity. With the gradual improvement of catalyst performance and cost reduction, dodecahydro-*N*-ethylcarbazole as a hydrogen source system in LOHCs for on-board fuel cells will become more competitive.

#### Conflicts of interest

There are no conflicts to declare.

#### Acknowledgments

The authors greatly appreciate the following financial supports: National Natural Science Foundation of China (No. 21706203), China Postdoctoral Science Foundation (2016M592794 and 2017T100754), Natural Science Basic Research Plan in Shaanxi Province of China (2017JQ2030), Postdoctoral Science Foundation in Shaanxi Province of China (2016BSHEDZZ20), Fundamental Research Funds for the Central Universities (xjj2018035 and Creative Team Plan No. cxtd2017004 in Xi'an Jiaotong University), research funding from the Joint Laboratory of Xi'an Jiaotong Univ. and Shaanxi Coal Chemical Industry Technology Research Institute Co. Ltd. The authors would like to thank Dr. Jiao Li, Engineer Jiamei Liu and Engineer Yu Wang at Instrument Analysis Center of Xi'an Jiaotong University, who provided guidance of characterization. The authors would like to thank Mr. Xin Chen from Anhui Kemi Machinery Technology Co., Ltd., who provided help during the installation and commissioning of the hydrogenation equipment.

#### References

- [1] B. Obama, The irreversible momentum of clean energy, *Science* 355 (2017)

- 126–129.
- [2] E. Gianotti, M. Taillades-Jacquín, J. Rozière, D.J. Jones, High-purity hydrogen generation via dehydrogenation of organic carriers: a review on the catalytic process, *ACS Catal.* 8 (2018) 4660–4680.
- [3] L. Schlapbach, A. Züttel, Hydrogen-storage materials for mobile applications, *Nature* 414 (2001) 353–358.
- [4] Q.L. Zhu, Q. Xu, Liquid organic and inorganic chemical hydrides for high-capacity hydrogen storage, *Energy Environ. Sci.* 8 (2015) 478–512.
- [5] J.D. Holladay, J. Hu, D.L. King, Y. Wang, An overview of hydrogen production technologies, *Catal. Today* 139 (2009) 244–260.
- [6] F.H. Saadi, N.S. Lewis, E.W. McFarland, Relative costs of transporting electrical and chemical energy, *Energy Environ. Sci.* 11 (2018) 469–475.
- [7] DOE Technical Targets for Onboard Hydrogen Storage for Light-Duty Vehicles, (2019).
- [8] M. Markiewicz, Y.Q. Zhang, A. Bösmann, N. Brückner, J. Thöming, P. Wasserscheid, S. Stolte, Environmental and health impact assessment of Liquid Organic Hydrogen Carrier (LOHC) systems – challenges and preliminary results, *Energy Environ. Sci.* 8 (2015) 1035–1045.
- [9] J. Yang, A. Sudik, C. Wolverton, D.J. Siegel, High capacity hydrogen storage materials: attributes for automotive applications and techniques for materials discovery, *Chem. Soc. Rev.* 39 (2010) 656–675.
- [10] P. Preuster, C. Papp, P. Wasserscheid, Liquid organic hydrogen carriers (LOHCs): toward a hydrogen-free hydrogen economy, *Acc. Chem. Res.* 50 (2017) 74–85.
- [11] G.P. Pez, A.R. Scott, A.C. Cooper, H. Cheng, Hydrogen storage by reversible hydrogenation of pi-conjugated substrates, *Google Patents*, 2008.
- [12] M.C. Williams, J.P. Strakey, W.A. Surdovall, The US department of energy, office of fossil energy stationary fuel cell program, *J. Power Sources* 143 (2005) 191–196.
- [13] G. Pez, A. Scott, A. Cooper, H. Cheng, US patent, 7101530, September, 2006.
- [14] M. Yang, C.Q. Han, G. Ni, J.P. Wu, H.S. Cheng, Temperature controlled three-stage catalytic dehydrogenation and cycle performance of perhydro-9-ethylcarbazole, *Int. J. Hydrogen Energy* 37 (2012) 12839–12845.
- [15] M. Yang, Y. Dong, S.X. Fei, Q.Y. Pan, G. Ni, C.Q. Han, H.Z. Ke, Q. Fang, H.S. Cheng, Hydrogenation of *N*-propylcarbazole over supported ruthenium as a new prototype of liquid organic hydrogen carriers (LOHC), *RSC Adv.* 3 (2013) 24877–24881.
- [16] F. Sotoodeh, K.J. Smith, Kinetics of hydrogen uptake and release from heteroaromatic compounds for hydrogen storage, *Ind. Eng. Chem. Res.* 49 (2010) 1018–1026.
- [17] K. Morawa Eblagon, K. Tam, K.M.K. Yu, S.-L. Zhao, X.-Q. Gong, H. He, L. Ye, L.-C. Wang, A.J. Ramirez-Cuesta, S.C. Tsang, Study of catalytic sites on ruthenium for hydrogenation of *N*-ethylcarbazole: implications of hydrogen storage via reversible catalytic hydrogenation, *J. Phys. Chem. C* 114 (2010) 9720–9730.
- [18] S. Fei, B. Han, L. Li, P. Mei, T. Zhu, M. Yang, H. Cheng, A study on the catalytic hydrogenation of *N*-ethylcarbazole on the mesoporous Pd/MoO<sub>3</sub> catalyst, *Int. J. Hydrogen Energy* 42 (2017) 25942–25950.
- [19] K.M. Eblagon, S.C.E. Tsang, Structure-reactivity relationship in catalytic hydrogenation of heterocyclic compounds over ruthenium black-part A: effect of substitution of pyrrole ring and side chain in *N*-heterocycles, *Appl. Catal. B-Environ.* 160 (2014) 22–34.
- [20] F. Sotoodeh, L. Zhao, K.J. Smith, Kinetics of H<sub>2</sub> recovery from dodecahydro-*N*-ethylcarbazole over a supported Pd catalyst, *Appl. Catal. A* 362 (2009) 155–162.
- [21] M. Yang, Y. Dong, S.X. Fei, H.Z. Ke, H.S. Cheng, A comparative study of catalytic dehydrogenation of perhydro-*N*-ethylcarbazole over noble metal catalysts, *Int. J. Hydrogen Energy* 39 (2014) 18976–18983.
- [22] M. Amende, S. Schernich, M. Sobota, I. Nikiforidis, W. Hieringer, D. Assenbaum, C. Gleichweit, H.J. Drescher, C. Papp, H.P. Steinruck, A. Gorling, P. Wasserscheid, M. Laurin, J. Libuda, Dehydrogenation mechanism of liquid organic hydrogen carriers: dodecahydro-*N*-ethylcarbazole on Pd(111), *Chemistry* 19 (2013) 10854–10865.
- [23] M. Sobota, I. Nikiforidis, M. Amende, B. Sanmartin Zanon, T. Staudt, O. Hofert, Y. Lykhach, C. Papp, W. Hieringer, M. Laurin, D. Assenbaum, P. Wasserscheid, H.P. Steinruck, A. Gorling, J. Libuda, Dehydrogenation of dodecahydro-*N*-ethylcarbazole on Pd/Al<sub>2</sub>O<sub>3</sub> model catalysts, *Chemistry* 17 (2011) 11542–11552.
- [24] L.M. Kustov, A.L. Tarasov, O.A. Kirichenko, Microwave-activated dehydrogenation of perhydro-*N*-ethylcarbazole over bimetallic Pd-M/TiO<sub>2</sub> catalysts as the second stage of hydrogen storage in liquid substrates, *Int. J. Hydrogen Energy* 42 (2017) 26723–26729.
- [25] M. Amende, C. Gleichweit, K. Werner, S. Schernich, W. Zhao, M.P. Lorenz, O. Hofert, C. Papp, M. Koch, P. Wasserscheid, M. Laurin, H.P. Steinruck, J. Libuda, Model catalytic studies of liquid organic hydrogen carriers: dehydrogenation and decomposition mechanisms of Dodecahydro-*N*-ethylcarbazole on Pt(111), *ACS Catal.* 4 (2014) 657–665.
- [26] M. Amende, C. Gleichweit, S. Schernich, O. Hofert, M.P. Lorenz, W. Zhao, M. Koch, K. Obesser, C. Papp, P. Wasserscheid, H.P. Steinruck, J. Libuda, Size and structure effects controlling the stability of the liquid organic hydrogen carrier dodecahydro-*N*-ethylcarbazole during dehydrogenation over Pt model catalysts, *J. Phys. Chem. Lett.* 5 (2014) 1498–1504.
- [27] Z. Wang, I. Tonks, J. Belli, C.M. Jensen, Dehydrogenation of *N*-ethyl perhydrocarbazole catalyzed by PCP pincer iridium complexes: evaluation of a homogeneous hydrogen storage system, *J. Organomet. Chem.* 694 (2009) 2854–2857.
- [28] D. Forberg, T. Schwob, M. Zaheer, M. Friedrich, N. Miyajima, R. Kempe, Single-catalyst high-weight% hydrogen storage in an *N*-heterocycle synthesized from lignin hydrogenolysis products and ammonia, *Nat. Commun.* 7 (2016) 13201.
- [29] S. Rostamnia, E. Doustkhah, H. Golchin-Hosseini, B. Zeynizadeh, H. Xin, R. Luque, Efficient tandem aqueous room temperature oxidative amidations catalysed by supported Pd nanoparticles on graphene oxide, *Catal. Sci. Technol.* 6 (2016) 4124–4133.
- [30] S. Rostamnia, E. Doustkhah, Z. Karimi, S. Amini, R. Luque, Surfactant-exfoliated

- highly dispersive Pd-Supported graphene oxide nanocomposite as a catalyst for aerobic aqueous oxidations of alcohols, *Chemcatchem* 7 (2015) 1678–1683.
- [31] M. Heidarizadeh, E. Doustkhah, S. Rostamnia, P.F. Rezaei, F.D. Harzevili, B. Zeynizadeh, Dithiocarbamate to modify magnetic graphene oxide nanocomposite (Fe3O4-GO): a new strategy for covalent enzyme (lipase) immobilization to fabrication a new nanobiocatalyst for enzymatic hydrolysis of PNPD, *Int. J. Biol. Macromol.* 101 (2017) 696–702.
  - [32] E. Doustkhah, S. Rostamnia, Covalently bonded sulfonic acid magnetic graphene oxide: Fe3O4@GO-Pr-SO3H as a powerful hybrid catalyst for synthesis of indazolophthalazinetriones, *J. Colloid Interface Sci.* 478 (2016) 280–287.
  - [33] S. Rostamnia, B. Zeynizadeh, E. Doustkhah, H.G. Hosseini, Exfoliated Pd decorated graphene oxide nanosheets (PdNP-GO/P123): non-toxic, ligandless and recyclable in greener Hiyama cross-coupling reaction, *J. Colloid Interface Sci.* 451 (2015) 46–52.
  - [34] S. Rostamnia, E. Doustkhah, B. Zeynizadeh, Exfoliation effect of PEG-type surfactant on Pd supported GO (SE-Pd(nanoparticle)/GO) in cascade synthesis of amides: a comparison with Pd(nanoparticle)/rGO, *J. Mol. Catal. A Chem.* 416 (2016) 88–95.
  - [35] B. Wang, T. Yan, T. Chang, J. Wei, Q. Zhou, S. Yang, T. Fang, Palladium supported on reduced graphene oxide as a high-performance catalyst for the dehydrogenation of dodecahydro- N -ethylcarbazole, *Carbon* 122 (2017) 9–18.
  - [36] B. Wang, T.-y. Chang, Z. Jiang, J.-j. Wei, Y.-h. Zhang, S. Yang, T. Fang, Catalytic dehydrogenation study of dodecahydro-N-ethylcarbazole by noble metal supported on reduced graphene oxide, *Int. J. Hydrogen Energy* 43 (2018) 7317–7325.
  - [37] B. Wang, T.-y. Chang, X. Gong, Z. Jiang, S. Yang, Y.-s. Chen, T. Fang, One-pot synthesis of Au/Pd Core/Shell nanoparticles supported on reduced graphene oxide with enhanced dehydrogenation performance for dodecahydro-N-ethylcarbazole, *ACS Sustain. Chem. Eng.* 7 (2018) 1760–1768.
  - [38] F. Zaera, Nanostructured materials for applications in heterogeneous catalysis, *Chem. Soc. Rev.* 42 (2013) 2746–2762.
  - [39] Z.-L. Wang, J.-M. Yan, H.-L. Wang, Y. Ping, Q. Jiang, Au@Pd core-shell nanoclusters growing on nitrogen-doped mildly reduced graphene oxide with enhanced catalytic performance for hydrogen generation from formic acid, *J. Mater. Chem. A* 1 (2013) 12721.
  - [40] M.B. Gawande, A. Goswami, F.X. Felpin, T. Asefa, X. Huang, R. Silva, X. Zou, R. Zboril, R.S. Varma, Cu and Cu-based nanoparticles: synthesis and applications in catalysis, *Chem. Rev.* 116 (2016) 3722–3811.
  - [41] C. Hu, Y. Guo, J. Wang, L. Yang, Z. Yang, Z. Bai, J. Zhang, K. Wang, K. Jiang, Additive-free fabrication of spherical hollow palladium/copper alloyed nanostructures for fuel cell application, *ACS Appl. Mater. Interface* 4 (2012) 4461–4464.
  - [42] C. Xu, Y. Liu, J. Wang, H. Geng, H. Qiu, Fabrication of nanoporous Cu–Pt (Pd) core/shell structure by galvanic replacement and its application in electrocatalysis, *ACS Appl. Mater. Interface* 3 (2011) 4626–4632.
  - [43] L. Zhang, F. Hou, Y. Tan, Shape-tailoring of CuPd nanocrystals for enhancement of electro-catalytic activity in oxygen reduction reaction, *Chem. Commun.* 48 (2012) 7152–7154.
  - [44] M. Shao, K. Shoemaker, A. Peles, K. Kaneko, L. Protsailo, Pt monolayer on porous Pd – Cu alloys as oxygen reduction electrocatalysts, *J. Am. Chem. Soc.* 132 (2010) 9253–9255.
  - [45] M. Yamauchi, R. Abe, T. Tsukuda, K. Kato, M. Takata, Highly selective ammonia synthesis from nitrate with photocatalytically generated hydrogen on CuPd/TiO2, *J. Am. Chem. Soc.* 133 (2011) 1150–1152.
  - [46] S.F. Ho, A. Mendoza-Garcia, S. Guo, K. He, D. Su, S. Liu, O. Metin, S. Sun, A facile route to monodisperse MPd (M = Co or Cu) alloy nanoparticles and their catalysis for electrooxidation of formic acid, *Nanoscale* 6 (2014) 6970–6973.
  - [47] S.E. Allen, R.R. Walvoord, R. Padilla-Salinas, M.C. Kozlowski, Aerobic copper-catalyzed organic reactions, *Chem. Rev.* 113 (2013) 6234–6458.
  - [48] Z.-Y. Shih, A.P. Periasamy, P.-C. Hsu, H.-T. Chang, Synthesis and catalysis of copper sulfide/carbon nanodots for oxygen reduction in direct methanol fuel cells, *Appl. Catal. B* 132 (2013) 363–369.
  - [49] G. Yin, M. Nishikawa, Y. Nosaka, N. Srinivasan, D. Atarashi, E. Sakai, M. Miyauchi, Photocatalytic carbon dioxide reduction by copper oxide nanocluster-grafted niobate nanosheets, *ACS Nano* 9 (2015) 2111–2119.
  - [50] Y. Zhu, X. Kong, X. Li, G. Ding, Y. Zhu, Y.-W. Li, Cu nanoparticles inlaid mesoporous Al2O3 as a high-performance bifunctional catalyst for ethanol synthesis via dimethyl oxalate hydrogenation, *ACS Catal.* 4 (2014) 3612–3620.
  - [51] R.V. Gonçalves, R. Wojcieszak, H. Wender, C. Sato B. Dias, L.L. Vono, D. Eberhardt, S.R. Teixeira, L.M. Rossi, Easy access to metallic copper nanoparticles with high activity and stability for CO oxidation, *ACS Appl. Mater. Interface* 7 (2015) 7987–7994.
  - [52] Y. Zheng, S. Zhao, S. Liu, H. Yin, Y.Y. Chen, J. Bao, M. Han, Z. Dai, Component-controlled synthesis and assembly of Cu-Pd nanocrystals on graphene for oxygen reduction reaction, *ACS Appl. Mater. Interfaces* 7 (2015) 5347–5357.
  - [53] S. Diyarbakir, H. Can, Ö. Metin, Reduced graphene oxide-supported CuPd alloy nanoparticles as efficient catalysts for the sonogashira cross-coupling reactions, *ACS Appl. Mater. Interface* 7 (2015) 3199–3206.
  - [54] Q.L. Zhang, J.N. Zheng, T.Q. Xu, A.J. Wang, J. Wei, J.R. Chen, J.J. Feng, Simple one-pot preparation of Pd-on-Cu nanocrystals supported on reduced graphene oxide for enhanced ethanol electrooxidation, *Electrochim. Acta* 132 (2014) 551–560.
  - [55] Q. Dong, Y. Zhao, X. Han, Y. Wang, M.C. Liu, Y. Li, Pd/Cu bimetallic nanoparticles supported on graphene nanosheets: facile synthesis and application as novel electrocatalyst for ethanol oxidation in alkaline media, *Int. J. Hydrogen Energy* 39 (2014) 14669–14679.
  - [56] M. Yuan, A.P. Liu, M. Zhao, W.J. Dong, T.Y. Zhao, J.J. Wang, W.H. Tang, Bimetallic PdCu nanoparticle decorated three-dimensional graphene hydrogel for non-enzymatic amperometric glucose sensor, *Sens. Actuators B-Chem.* 190 (2014) 707–714.
  - [57] M. Kumar, S. Deka, Multiply twinned AgNi alloy nanoparticles as highly active catalyst for multiple reduction and degradation reactions, *ACS Appl. Mater. Interfaces* 6 (2014) 16071–16081.
  - [58] D. Bin, B.B. Yang, F.F. Ren, K. Zhang, P. Yang, Y.K. Du, Facile synthesis of PdNi nanowire networks supported on reduced graphene oxide with enhanced catalytic performance for formic acid oxidation, *J. Mater. Chem. A* 3 (2015) 14001–14006.
  - [59] R.F. Nie, J.H. Wang, L.N. Wang, Y. Qin, P. Chen, Z.Y. Hou, Platinum supported on reduced graphene oxide as a catalyst for hydrogenation of nitroarenes, *Carbon* 50 (2012) 586–596.
  - [60] H. Wang, Y.F. Wang, X.W. Cao, M. Feng, G.X. Lan, Vibrational properties of graphene and graphene layers, *J. Raman Spectrosc.* 40 (2009) 1791–1796.
  - [61] Y.Z. Li, Y. Yu, J.G. Wang, J. Song, Q. Li, M.D. Dong, C.J. Liu, CO oxidation over graphene supported palladium catalyst, *Appl. Catal. B-Environ* 125 (2012) 189–196.
  - [62] C. Xu, X. Wang, J. Zhu, Graphene – Metal particle nanocomposites, *J. Phys. Chem. C* 112 (2008) 19841–19845.
  - [63] P. Liu, E.J. Hensen, Highly efficient and robust Au/MgCuCr2O4 catalyst for gas-phase oxidation of ethanol to acetaldehyde, *J. Am. Chem. Soc.* 135 (2013) 14032–14035.
  - [64] I. Platzman, R. Brenner, H. Haick, R. Tannenbaum, Oxidation of polycrystalline copper thin films at ambient conditions, *J. Phys. Chem. C* 112 (2008) 1101–1108.
  - [65] Y. Li, Y. Li, E. Zhu, T. McLouth, C.Y. Chiu, X. Huang, Y. Huang, Stabilization of high-performance oxygen reduction reaction Pt electrocatalyst supported on reduced graphene oxide/carbon black composite, *J. Am. Chem. Soc.* 134 (2012) 12326–12329.
  - [66] G.M. Scheuermann, L. Rumi, P. Steurer, W. Bannwarth, R. Mulhaupt, Palladium nanoparticles on graphite oxide and its functionalized graphene derivatives as highly active catalysts for the Suzuki-Miyaura coupling reaction, *J. Am. Chem. Soc.* 131 (2009) 8262–8270.
  - [67] Y.S. Lee, C.N. Whang, Y. Jeon, B.S. Choi, T.J. Han, J.J. Woo, M. Croft, Study of the L-3 edges of ion-beam-mixed Pd-Cu alloys by X-ray absorption spectroscopy, *Nuclear Instrum. Methods in Phys. Res. Sect. B-Beam Interactions Mater. Atoms* 129 (1997) 387–391.
  - [68] E.J. Cho, S. Lee, S. Oh, M. Han, S. Lee, C.N. Whang, Unoccupied states and charge transfer in Cu-Pd alloys studied by bremsstrahlung isochromat spectroscopy, x-ray photoelectron spectroscopy, and LIII absorption spectroscopy, *Phys. Rev. B Condens. Matter* 52 (1995) 16443–16450.
  - [69] E. Choi, S.J. Oh, M. Choi, Charge transfer in NiPt1 – x alloys studied by x-ray photoelectron spectroscopy, *Phys. Rev. B* 43 (1991) 6360–6368.